Coexistence of localized and collective magnetism in the coupled-spin-tetrahedra system $Cu_4Te_5O_{12}Cl_4$

Kwang-Yong Choi,[1,*] Seunghwan Do,[1] Peter Lemmens,[2] Johan van Tol,[3,4] Jiseon Shin,[5] Gun Sang Jeon,[5] Yurii Skourski,[6] Jong-Soo Rhyee,[7] and Helmuth Berger[8]

[1]*Department of Physics, Chung-Ang University, Seoul 156-756, Republic of Korea*
[2]*Institute for Condensed Matter Physics, TU Braunschweig, D-38106 Braunschweig, Germany*
[3]*Department of Chemistry and Biochemistry, Florida State University, Tallahassee, Florida 32306, USA*
[4]*National High Magnetic Field Laboratory, Florida State University, Tallahassee, Florida 32310, USA*
[5]*Department of Physics, Ewha Womans University, Seoul 120-750, Republic of Korea*
[6]*Dresden High Magnetic Field Laboratory, Forschungszentrum Dresden-Rossendorf, 01314 Dresden, Germany*
[7]*Department of Applied Physics, Kyung Hee University, Yongin 446-701, Republic of Korea*
[8]*Institute de Physique de la Matiere Complexe, EPFL, CH-1015 Lausanne, Switzerland*

(Received 4 July 2014; revised manuscript received 28 September 2014; published 3 November 2014)

We report high-field magnetization, electron spin resonance (ESR), and Raman scattering measurements of the coupled spin-tetrahedra system $Cu_4Te_5O_{12}Cl_4$ with magnetic ordering at $T_N = 13.6$ K. We find thermodynamic and spectroscopic signatures for the concomitant occurrence of localized and collective magnetism. Magnetization measurements up to 60 T exhibit a spin-flop transition at $\mu_0 H_{SF} = 16$ T only for $H \| c$ as well as periodic magnetization steps at $\mu_0 H = 16.5$, 24.8, 33.8, 42.3, and 49.7 T, which are independent of the crystallographic orientations. For $T > T_N$, the temperature dependence of ESR linewidth is described by a critical power law, $\Delta B_{pp}(T) \propto (T - T_N)^{-0.56\pm0.02}$. For $T < T_N$, an antiferromagnetic resonance mode is observed for $H \| c$, and its linewidth is given by $\Delta B_{pp}(T) \propto T^{3.13\pm0.04}$, being close to T^4 expected for a classical magnet. Raman spectra show three one-magnon-like excitations superimposed on a broad two-magnon continuum. While the two higher frequency modes show an intensity variation in accordance to a three-dimensional Heisenberg antiferromagnet, the lower frequency mode clearly deviates. These results suggest that $Cu_4Te_5O_{12}Cl_4$ is a unique material which shows a dual character of zero-dimensional, localized and three-dimensional, collective magnetic behaviors.

DOI: 10.1103/PhysRevB.90.184402 PACS number(s): 75.10.Jm, 64.70.Tg, 75.30.Ds

I. INTRODUCTION

Coupled spin-tetrahedra systems have proven to be a versatile reservoir to explore the crossover from localized spin dynamics to a more collective behavior. When intra- and intertetrahedral interactions compete with each other, there emerge a variety of interesting phenomena [1–3]. This showed up in the low-energy excitations, which constitute transverse (Goldstone) and longitudinal magnon (Higgs) modes along with gapped singlet excitations [4].

To date, only a handful of materials $Cu_2Te_2O_5X_2$ (X = Br, Cl) [designated as Cu2252], $Cu_4Te_5O_{12}Cl_4$ (designated as Cu45124), $K_4Cu_4OCl_{10}$, and $CuSeO_3$ have been known to realize such coupled tetrahedra [5–8]. In the last decade, research on spin tetrahedra systems has predominantly focused on the oxohalide Cu2252 family, in which four Cu^{2+} spins form a distorted tetrahedron aligned in chains along the c axis and are separated by lone-pair ions within the ab plane [5]. The Br and Cl compounds undergo an incommensurate magnetic ordering at $T_N = 11$ and 18 K, respectively [1]. Despite the fact that both compounds share the same magnetic structure, marked differences in magnetic excitations and spin dynamics were found between them [9–22]. The Cl compound was largely described by a classical magnet while the Br compound was considered to lie in close proximity to a quantum critical point. Even for the case of the Cl compound, showing an apparent classical behavior, a mean-field or random-phase approximation theory failed to account for inelastic neutron scattering spectra [4]. This has spurred a debate on the role of spatially anisotropic intertetrahedral exchange interactions in these materials, calling for further investigations of more isotropically coupled spin tetrahedra.

Cu45124 is regarded as an isotropic cousin of Cu2252 which has a noncentrosymmetric space group $P\bar{4}$. Three-dimensional (3D) arrangements of spin tetrahedra in Cu45124 are due to the centrosymmetric tetragonal structure (space group $P4/n$) and allow for the examination of intrinsic features to the 3D coupled zero-dimensional (0D) spin clusters.

Cu2252 and Cu45124 have the $[CuO_3Cl]$ distorted square as a common structural unit. A corner-sharing of four such squares leads to the formation of a Cu tetrahedron as sketched in Fig. 1(a). The major structural difference between the two compounds is the presence of a $Te(1)O_4$ complex for Cu45124, which connects Cu tetrahedra in the ab plane [see Fig. 1(b)]. In comparison to Cu2252, this structural change leads to the reduction of intratetrahedral and in-plane diagonal intertetrahedral interactions while strengthening out-of-plane intertetrahedral couplings [23]. This indicates that a magnetic dimensionality is increased and anisotropic exchange contributions are diminished in Cu45124. Magnetic susceptibility and specific-heat data exhibit an antiferromagnetic long-range ordering at $T_N = 13.6$ K [6]. Consistently with first-principle calculations [23], the overall energy scale of magnetic Raman excitations is reduced as compared to Cu2252.

In this paper, we employ high-field magnetization, electron spin resonance (ESR), and Raman spectroscopy to investigate the magnetic properties of Cu45124, a more three-dimensional

*kchoi@cau.ac.kr

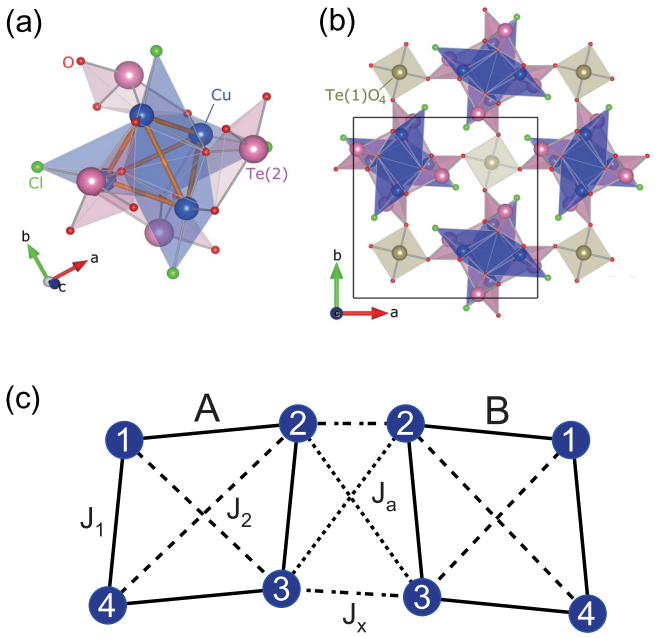

FIG. 1. (Color online) (a) Sketch of a tetrahedron of Cu^{2+} with local environments. The pink, olive, blue, green, and red balls stand for Te(1), Te(2), Cu, Cl, and O atoms, respectively. (b) Crystal structure of $Cu_4Te_5O_{12}Cl_4$ projected on the ab plane. [CuO_4Cl] tetrahedra, Te(1)O_4 pyramids, and Te(2)O_4 polyhedra are represented by blue, olive, and pink shaded colors, respectively. (c) Schematic description of the spin models adopted in numerical calculation with intratetrahedral coupling constants J_1 (solid lines) and J_2 (dashed lines) as well as two intertetrahedral coupling constants J_a (dotted lines) and J_x (dotted-dashed lines). The blue balls indicate $S = 1/2$ Cu^{2+} ions.

counterpart of Cu2252. We provide evidence for coexistence of both localized and collective magnetism, signatures of the respective zero and three dimensionality. This coexistence is not evident for the case of Cu2252, which has spatially anisotropic intertetrahedral exchange interactions.

II. EXPERIMENTAL DETAILS

$Cu_4Te_5O_{12}Cl_4$ single crystals were grown with chemical transport in sealed, evacuated silica tubes [6]. Magnetic susceptibility was measured in a temperature range of $T =$ 2–50 K under applied fields of $\mu_0 H = 1$–13 T using a Quantum Design PPMS Dynacool VSM (vibrating sample magnetometer). High-field magnetization measurements were performed at the Dresden High Magnetic Field Laboratory using a pulsed field magnet (20 ms duration) and an induction method with a pick-up coil device at $T = 1.5$ K in a field range of $\mu_0 H = 0$–60 T. High-frequency ESR experiments were carried out at $\nu = 240$ GHz using a quasioptical spectrometer and sweepable 12-T superconducting magnet. The spectrometer employed a superheterodyne detection scheme with a lock-in amplifier for field modulation. Consequently, the field derivative of a microwave absorption signal was recorded as a function of the sweeping magnetic field. Polarized Raman-scattering experiments were performed in quasibackscattering geometry using a solid state laser ($\lambda = 532.1$ nm, $P = 1$ mW). The samples were installed into a He-cooled closed cycle cryostat with a temperature range of $T = 3$–300 K. The spectra were collected via a Dilor-XY 500 triple spectrometer equipped with a nitrogen cooled charge-coupled device detector.

III. RESULTS AND DISCUSSION

A. Magnetic susceptibility and high field magnetization

Figure 2 presents the field dependence of the dc magnetic susceptibility $\chi(T) = M/B$ for $H \| a$, measured in a low-temperature range of $T = 2$–25 K. With decreasing temperature $\chi(T)$ shows a broad maximum around $T_{max} = 18$ K and, subsequently, a small kink at $T_N = 13.6$ K, as indicated by the arrow and, finally, drops to a finite residual value as $T \to 0$. The broad maximum is related to the onset of short-range antiferromagnetic ordering, typical for frustrated spin systems. The kink feature indicates a transition to the long-range ordered state for $T < T_N$.

Applying an external field, the maximum position of $\chi(T)$ shifts slightly to lower temperature but the transition temperature, identified by taking the derivative of $\chi(T)$, shows a nonmonotonic field dependence. As plotted in the inset of Fig. 2, T_N slightly increases as the field is raised up to 5 T and then undergoes a slight decrease for $\mu_0 H > 5$ T. We recall that Cu2252-Cl showed a small decrease of T_N with increasing H, which is consistent with a classical antiferromagnet [1,10]. This is contrasted by the increase of T_N with an applied field, for Cu2252-Br, which was discussed in terms of dominant singlet fluctuations. Since single-ion anisotropies of Cu^{2+} ions are negligible, the observed field dependence of T_N for Cu45124 may result from the competition between 3D magnetic ordering and 0D singlet fluctuations.

Shown in Fig. 3 is the high-field magnetization curve $M(B)$ measured at $T = 1.5$ K for $H \| c$ and $H \| a$ using a pulsed field magnet. $M(B)$ exhibits a concave curvature with fine structures up to 60 T. $M(B)$ is anisotropic between $H \| c$ and $H \| a$ in lower fields while it becomes isotropic in higher fields. For

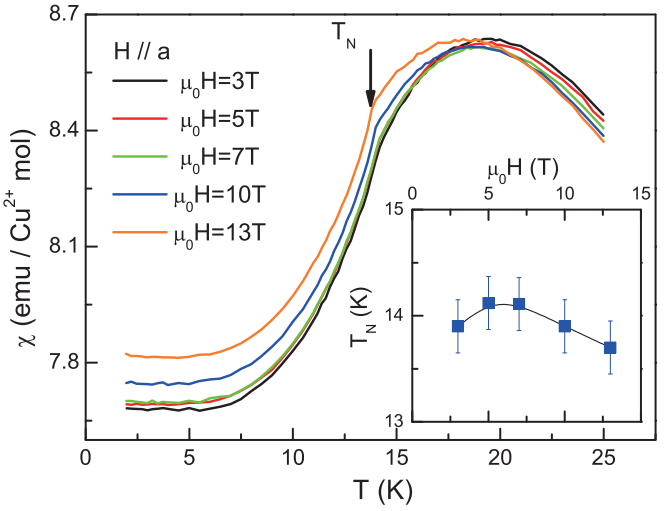

FIG. 2. (Color online) Temperature dependence of dc magnetic susceptibility of $Cu_4Te_5O_{12}Cl_4$ measured at $\mu_0 H = 1$–13 T for $H \| a$. The vertical arrow indicates a magnetic ordering transition at T_N. The inset plots the field dependence of T_N.

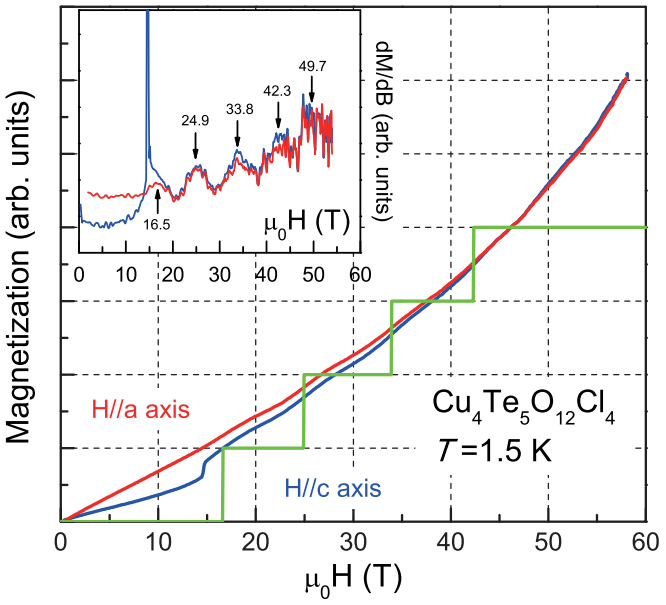

FIG. 3. (Color online) Magnetization vs pulsed magnetic field for $Cu_4Te_5O_{12}Cl_4$ measured at $T = 1.5$ K for $H\|c$ and $H\|a$. The green solid line represents the magnetization calculated numerically from the coupled-tetrahedra spin model sketched in Fig. 1(c). See the text for parameters. Inset: Derivative dM/dB of the magnetization. Five peaks in dM/dB correspond to magnetization jumps.

$H\|c$, a spin-flop transition is observed at $\mu_0 H_{SF} = 16$ T as a sharp jump. This is characteristic of an antiferromagnet when an external field is applied along an easy axis, implying that the c axis corresponds to a magnetic easy axis. Apart from the spin-flop transition, we find five weak magnetization jumps at $\mu_0 H = 16.5$, 24.8, 33.8, 42.3, and 49.7 T in the measured field range as evident from the derivative $dM(B)/dB$ (see the inset of Fig. 3). They are independent of the crystallographic orientations and are almost equally spaced. This indicates that the periodic magnetization steps arise from the discrete energy levels of spin tetrahedra. We note that a mean-field theory reproduced well an overall shape of $M(B)$ with a spin-flop transition in a coupled spin-tetrahedra system but could not capture magnetization steps [12].

We perform numerical calculations to examine the discrete levels of spin tetrahedra. With $S = 1/2$ Cu^{2+} distorted tetrahedra the spins interact with one another via exchange interactions. We introduce four different coupling constants: two intratetrahedral ones, J_1 and J_2, and two intertetrahedral ones, J_x and J_a, as depicted in Fig. 1(c). The spin Hamiltonian of two coupled tetrahedra is given in periodic boundary conditions by

$$\mathcal{H} = \sum_{\alpha=A,B}\left[J_1\sum_{i=1}^{4}\boldsymbol{S}_i^\alpha\cdot\boldsymbol{S}_{i+1}^\alpha + J_2\left(\boldsymbol{S}_1^\alpha\cdot\boldsymbol{S}_3^\alpha + \boldsymbol{S}_2^\alpha\cdot\boldsymbol{S}_4^\alpha\right)\right] + J_x\left[\sum_{i=1}^{4}\boldsymbol{S}_i^A\cdot\boldsymbol{S}_i^B + \sum_{\alpha}\left(\boldsymbol{S}_1^\alpha\cdot\boldsymbol{S}_3^{\bar\alpha} + \boldsymbol{S}_2^\alpha\cdot\boldsymbol{S}_4^{\bar\alpha}\right)\right] + 2J_a\sum_{\alpha}\left(\boldsymbol{S}_1^\alpha\cdot\boldsymbol{S}_3^{\bar\alpha} + \boldsymbol{S}_2^\alpha\cdot\boldsymbol{S}_4^{\bar\alpha}\right) - g\mu_0\mu_B\boldsymbol{H}\cdot\sum_{\alpha}\sum_{i=1}^{4}\boldsymbol{S}_i^\alpha, \quad (1)$$

where $\boldsymbol{S}_i^\alpha$ denotes the spin at ith site in tetrahedron α, and $\bar\alpha = A(B)$ for $\alpha = B(A)$ (note that $\boldsymbol{S}_5^\alpha \equiv \boldsymbol{S}_1^\alpha$ in the first term).

The above Hamiltonian commutes with $S_n \equiv \sum_{i\alpha}\boldsymbol{S}_i^\alpha\cdot\hat{n}$, where $\hat{n}$ is the unit vector along the direction of magnetic field $\boldsymbol{H}$, and the $\hat{n}$ component of total spin is a good quantum number. It is obvious that the energy of the mth eigenstate with S_n changes linearly with H,

$$E_m(S_n,\mu_0 H) = E_m(S_n,\mu_0 H = 0) - g\mu_0\mu_B H S_n. \quad (2)$$

For $\mu_0 H = 0$, the ground state lies in the Hilbert space with $S_n = 0$ while the energy of the state with higher S_n decreases faster. Accordingly, we can expect that the system undergoes successive transitions to the states with higher values of S_n.

The procedure of numerical calculations is as follows: For a set of coupling constants $\{J_1, J_2, J_x, J_a\}$ we diagonalize the Hamiltonian in Eq. (1) numerically within the Hilbert space of $S_n = -4, -3, \ldots, 4$, respectively, yielding $\{E_m(S_n,\mu_0 H = 0)\}$. Using Eq. (2), we can determine the ground state in the presence of magnetic field H. We calculate the magnetic fields where quantum phase transitions occur between the states with different S_n, which correspond to the magnetization jumps observed in experiments. We vary the values of coupling constants and obtain the optimal set, $J_1 = 25.1$ K, $J_2 = 17.6$ K, $J_x = 23.8$ K, and $J_a = 26.4$ K, which reproduces best the experimentally observed magnetization jumps. Figure 4 shows the energy levels of the eigenstates as a function of H for the optimal set of exchange couplings. As is expected, four successive transitions from $S_n = 0$ to $S_n = 4$ occurs, resulting in four magnetic jumps.

The green line in Fig. 3 represents the numerical result for S_n with the variation of H. The numerical results capture nicely the first four periodic magnetization jumps, corroborating a quantized nature of the observed magnetization steps. It is worthwhile to mention that the two-tetrahedron model can explain only the first four jumps because in the model the total spin S_n is limited to 4. It is expected that the cluster with more

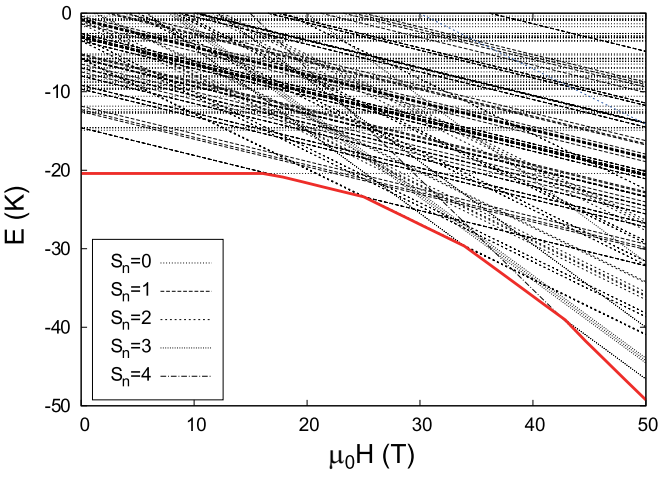

FIG. 4. (Color online) Energy (per spin) of the eigenstates of a two-tetrahedron cluster as a function of magnetic field. The energy of the ground state is represented by a thick (red) solid line. As the magnetic field is increased, the total spin S_n of the ground state increases. Magnetization shows a jump at the magnetic field where a lower-spin state undergoes a transition to a higher-spin one.

tetrahedra can give the jumps at higher magnetic fields as well as can yield the smooth magnetization jumps as observed in the experiment.

The estimated J_1 in this work turns out to be a little smaller than that from the earlier study, 32.9 K, which is estimated from $\chi(T)$ based on the isolated tetrahedra model [6]. It is of interest to note that the intertetrahedral coupling constants, J_x and J_a are comparable to the intratetrahedral ones. Complementary to the mean-field theory, our cluster-based calculation allows for the identification of the magnetization steps. However, it is beyond the scope of the present study to account for the concomitant spin-flop and magnetization steps of $M(B)$.

B. Electron spin resonance

To investigate the development of spin correlations we employed a high-frequency ESR technique at $\nu = 240$ GHz. In Fig. 5 we present the temperature dependence of ESR spectra for $H \| c$, i.e., an easy-axis direction. Each spectrum is scaled to unity. At room temperature we observe a broad signal described by a single Lorentzian absorption profile. This implies that the ESR linewidth is exchange-narrowed due to fast electronic fluctuations induced by an exchange interaction between the Cu^{2+} ions. The g factor is evaluated from the relation $g_c = h\nu/\mu_B B_{\rm res} = 2.104 \pm 0.006$ where μ_B is the Bohr magneton and $B_{\rm res} = 8.149 \pm 0.003$ T is the resonance field. The obtained g value is typical for a copper ion with a quenched orbital moment.

As the temperature is lowered, the spectrum undergoes a broadening and a shift to lower field. In the vicinity of T_N, the ESR signal wipes out and reappears for temperatures below T_N. Upon cooling below 10 K, the spectrum narrows substantially and shifts strongly toward higher field. To analyze their evolution, we extracted the resonance field ($B_{\rm res}$) and the peak-to-peak linewidth (ΔB_{pp}) by fitting to a Lorentzian profile. The resulting $B_{\rm res}(T)$ and $\Delta B_{pp}(T)$ are plotted in Fig. 6 as a function of temperature.

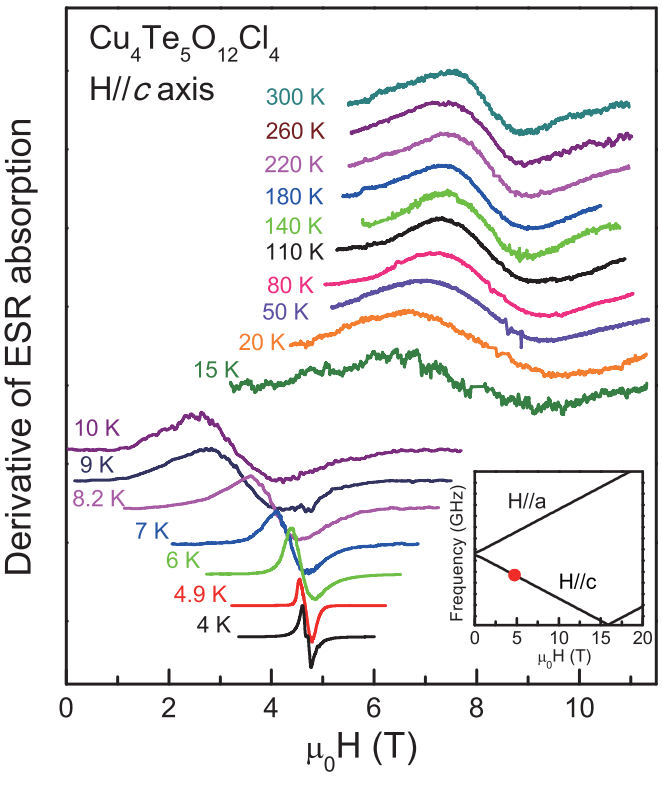

FIG. 5. (Color online) Derivative of the ESR absorption spectra of $Cu_4Te_5O_{12}Cl_4$ measured at $\nu = 240$ GHz for $H \| c$ as a function of temperature. The spectra are scaled to unity and are vertically shifted for clarity.

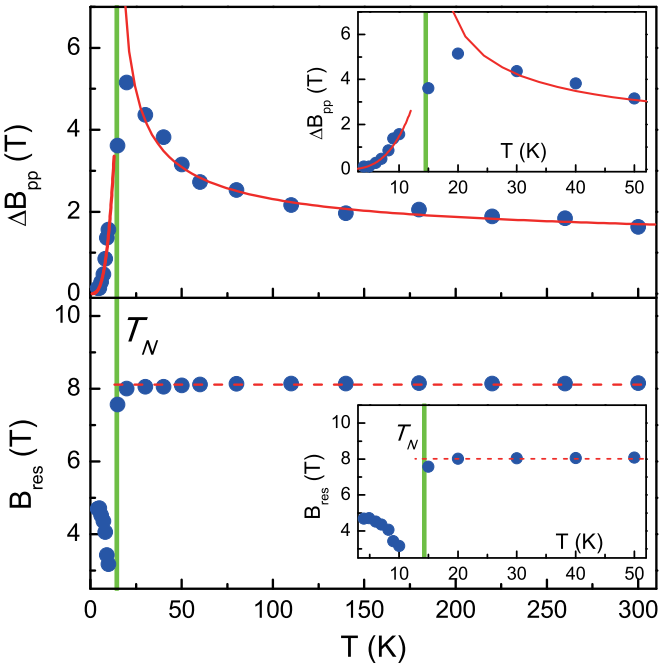

FIG. 6. (Color online) Temperature dependence of the peak-to-peak ESR linewidth $\Delta B_{pp}(T)$ (upper panel) and the resonance field $B_{\rm res}(T)$ (lower panel). Inset: A zoom of $\Delta B_{pp}(T)$ and $B_{\rm res}(T)$ at low temperatures. The solid lines are a fit of $\Delta B_{pp}(T)$ to a power law as described in the text. The dashed line is a guide to the eye.

The linewidth is very broad even at room temperature and amounts to $\Delta B_{pp}(300\ {\rm K}) = 1.635 \pm 0.004$ T. As the temperature approaches T_N, $\Delta B_{pp}(T)$ exhibits a critical broadening while $B_{\rm res}(T)$ is T independent for temperatures down to 20 K.

In the paramagnetic regime, the temperature dependence of the linewidth is given by $\Delta B_{pp}(\theta,T) = \alpha(\theta,T)\Delta B_{pp}(\theta,\infty)$ where $\Delta B_{pp}(\theta,\infty)$ is the linewidth in an uncorrelated high-temperature limit. For nonfrustrated classical magnets, $\Delta B_{pp}(T)$ is T independent in the paramagnetic state. For the studied compound, however, $\Delta B_{pp}(T)$ shows a strong T dependence in the whole measured temperature range. Such a behavior has been often reported in frustrated spin systems and is associated with the persistence of local spin correlations up to the Curie-Weiss temperature $\theta_{\rm CW}$ [24–26]. Noticeably, for Cu45124 the spin correlations persist to 30 $\theta_{\rm CW}$, indicating that $\theta_{\rm CW}$ does not provide a good energy scale for coupled zero-dimensional magnetism. We find that the broadening is well described by a critical power law, $\Delta B_{pp}(T) \propto (T - T_N)^{-p} + \Delta B_{pp}(\infty)$ with the exponent of $p = 0.56 \pm 0.02$ and $\Delta B_{pp}(\infty) = 1.062 \pm 0.006$ T (see the solid line in Fig. 6). The extracted critical exponent lies between $p \approx 0.3(9)$–$0.4(8)$ of the distorted triangular antiferromagnet $\alpha - CaCr_2O_4$ and

$p \approx 0.7(5)$ of the geometrically frustrated chain compound $FeTe_2O_5Br$ [25,26].

Next, we will turn to the antiferromagnetic resonance (AFMR) mode observed for temperatures below T_N. For an antiferromagnetically ordered magnet, the AFMR modes arise from spin-wave excitations by a microwave at $Q = 0, \pm q_{ICM}$. In the case of a two-sublattice antiferromagnet, two AFMR modes are allowed as sketched in the inset of Fig. 5. The lower resonance mode occurs when an external field is applied in an easy-axis direction, i.e., $H \| c$. The easy-axis AFMR mode softens to zero as the applied field is increased to $\mu_0 H_{SF}$. The observed AFMR mode is indicated by the full circle in a frequency-field diagram. Since the employed frequency is smaller than a zero-field gap, the higher resonance mode cannot be probed.

Upon cooling from T_N, the AFMR signal significantly narrows as $T \to 0$ and its resonance field shifts toward higher fields. The AFMR linewidth is determined by the population of magnons and follows a power law $\Delta B_{pp} \propto T^n$ with $n = 4$ for an antiferromagnet [27]. The linewidth of Cu45124 shows a power-law behavior $\Delta B_{pp}(T) \propto T^n$ with $n = 3.13 \pm 0.04$. The obtained exponent is close to the classical value of $n = 4$. This is contrasted to other frustrated magnets, which show a much smaller exponent of $n = 1.4$–2.2 [24–26]. The weaker T dependence is normally taken as evidence for persisting singlet fluctuations into the ordered state. Based on this observation, we conclude that Cu45124 behaves almost like a classical magnet in the ordered state due to the 3D intertetrahedral interactions. On the other hand, the large ΔB_{pp} and its T dependence persisting up to 30 θ_{CW} in the paramagnetic phase signal the significance of 0D spin fluctuations. This coexisting feature is also reflected in $M(B)$, which displays the spin-flop transition at lower field and the magnetization steps at higher field.

C. Phononic Raman spectra

Takagi *et al.* [6] have already reported Raman scattering measurements of Cu45124. In the previous study, however, the full spectrum of lattice and spin excitations could not have been elucidated due to the lack of sizable single crystals. Here we reinvestigated temperature dependence of lattice and magnetic excitations with a view of obtaining a better understanding of coupled tetrahedra.

Figure 7 compares the Raman spectra of Cu45124 measured at $T = 3$ K in (aa), (cc), and (ab) polarization. In these scattering configurations, we observe a total of 38 sharp modes in the frequency range 50–800 cm^{-1}. For the tetragonal $P4/n$ space group, the factor group analysis yields the total irreducible representation for Raman-active modes $\Gamma_{Raman} = 18A_g(aa,bb,cc) + 18B_g(aa,bb,ab) + 17E_g(bc,ca)$. In the measured scattering geometry, we expect $18A_g + 18B_g$ modes, which match well with the observed number of phonons. The surplus two peaks might be due to a polarization leakage.

Assigning symmetries and eigenvectors to the specific phonon modes is almost impossible because of a dense distribution of the phonon spectrum. Instead, we group the phonon modes into four spectral regimes in accordance with the frequency separation: 40–190 (I), 200–330 (II), 340–550 (III), and 600–800 cm^{-1} (IV). The high-energy IV modes involve

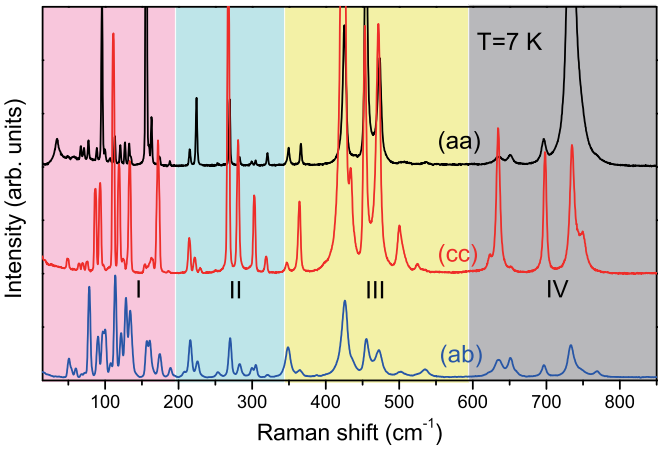

FIG. 7. (Color online) Comparison of Raman spectra in (aa), (cc), and (ab) polarization measured at $T = 3$ K, respectively.

the vibrations of the $[CuO_3Cl]$ blocks. The middle-energy III (II) modes contain the motions of Te, Cu, and O atoms where the lightest O (heaviest Te) atoms have the largest net atomic displacements. In the case of the group I, the Cl atoms, having a weak interaction with the other atoms, are mainly responsible for the lowest frequency modes.

Consistent with the previous study [6], the phonon modes do not show anomalous behavior and their temperature dependence is well described by weakly anharmonic displacements. Nonetheless, we find some indication of additional weak spin-phonon coupling.

In Fig. 8 we plot the frequency of the representative modes at 155 and 453 cm^{-1} as a function of temperature. The errors are within the symbol size. A tiny but discernible anomaly is observed for the 155-cm^{-1} mode in the vicinity of T_N. To discriminate the small effect, the temperature dependence of the frequency is fitted to a model based on phonon-phonon

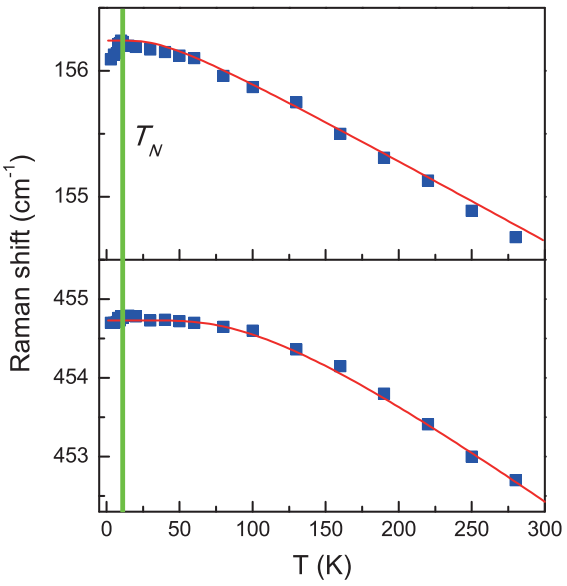

FIG. 8. (Color online) Temperature dependence of the frequency of phonon modes at 155 and 453 cm^{-1}. The solid lines are a fit to Eq. (3). The green vertical bar denotes the magnetic transition temperature.

decay processes [28],

$$\omega_{ph}(T) = \omega_0 + \frac{C}{1 + 2/(e^{\hbar\omega_0/2k_BT} - 1)}, \quad (3)$$

where ω_0 is the bare phonon frequency and C is the constant. This model provides a nice description to the experimental data over the whole temperature with $\omega_0 = 156.65 \pm 0.07$ (457.14 ± 0.05 cm^{-1}) and $C = -0.36 \pm 0.03$ (-2.27 ± 0.06) cm^{-1} for the 155 (453)-cm^{-1} mode. The tiny drop of the 155-cm^{-1} mode below T_N is due to magnetoelastic couplings. Such a tiny effect can be understood if taking into account the long, high symmetry of Cu-O-Te-O-Cu exchange paths and the compensation of spin-phonon couplings due to the existence of an inversion center.

D. Magnetic Raman scattering

We turn now to the magnetic excitations which show a marked variation in intensity and energy with temperature. We observe sharp three modes at 35 (marked as M_1), 40 (M_2), and 57 cm^{-1} (M_3) superimposed on a weak, broad continuum ($2M$) extending from 15 to 150 cm^{-1}, as shown in Fig. 9(a). We note that the third magnetic mode M_3 was not resolved in the earlier study [6].

In the Fleury-Loudon-Elliott approach [29], the magnetic Raman scattering intensity is proportional to $I_R \propto |\langle i|\sum_{i,j}\vec{S}_i\cdot\vec{S}_j|j\rangle|^2$. Inelastic scattering of an AFM ground state ($S = 1/2, S_z = \pm 1/2$) by light occurs via double spin-flip processes into a higher state ($S = 1/2, S_z = \mp 1/2$) since a Raman scattering process conserves the total spin of the z component ($S_z^{\rm tot} = 0$). The spectral weight of this two-magnon scattering is given by the density of states of a two-magnon spectrum, $\rho_2(\omega) = \sum_k \delta(\omega - 2\omega_k)$, where ω_k is a one-magnon dispersion. Based on the broad line shape and temperature dependence, the continuum is assigned to two-magnon scattering. The sharp M_i peaks disappear for $T > T_N$. This behavior is characteristic of one-magnon-like excitations. These zone-center transverse and longitudinal magnon modes are Raman active by virtue of spin-orbit coupling and/or anisotropic exchange interactions which manifest themselves in an exchange anisotropy [30]. Indeed, the spin-flop field of $\mu_0 H_{\rm SF} = 16$ T is surprisingly large in view of the nearly quenched orbital moment of the Cu^{2+} ion. This is suggestive of the large magnitude of the anisotropic part relative to the exchange interaction.

In Figs. 9(b) and 9(c) we present the detailed temperature dependence of the magnetic Raman scattering spectra after subtracting phonon peaks. Upon warming through T_N, the one-magnon M_i modes dissolve into a continuum of excitations. At high temperatures, the one- and two-magnon excitations turn into an intense quasielastic peak due to overdamped spin excitations. For a quantitative analysis we fit them to Gaussian profiles by taking into account the broad continuum. The representative fit is shown in Fig. 9(a). The resulting parameters are summarized in Fig. 10.

The energy of the M_i modes is plotted in Fig. 10(a) as a function of temperature. The temperature dependence of the peak energies is found to be described by the relation $E(T) = A(T - T_N)^\alpha + E_0$ with $\alpha = 0.49 \pm 0.05$, 0.54 ± 0.07, and 0.57 ± 0.05 for the respective M_i (i = 1–3). Since $I_R \propto \langle S_i S_j S_k S_l\rangle$, the intensity of the magnetic

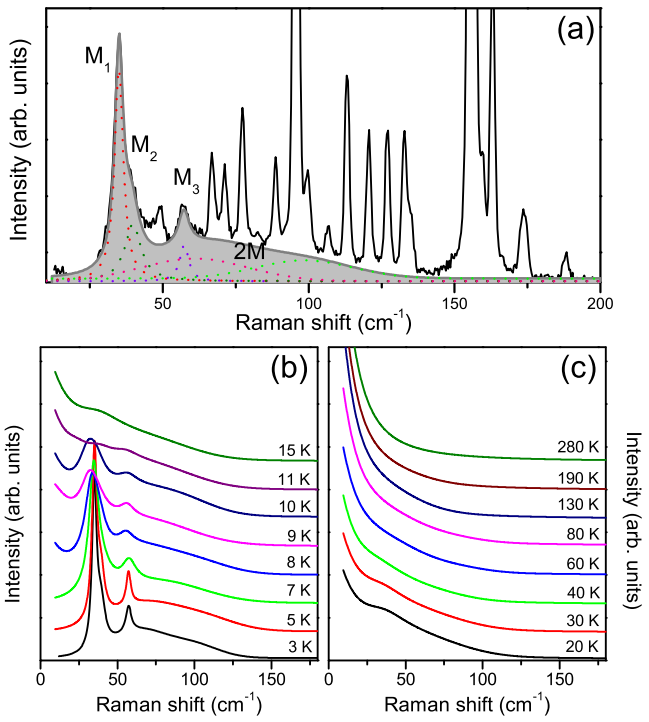

FIG. 9. (Color online) (a) Representative fit of $Cu_4Te_5O_{12}Cl_4$ at $T = 3$ K to Gaussian profiles. $M_i (i = 1–3)$ are the three sharp magnetic signals. The shaded region denotes a total magnetic contribution consisting of two-magnon continuum and three one-magnon-like excitations. (b) and (c) Temperature dependence of the low-energy magnetic Raman scattering obtained after subtracting all phonon modes.

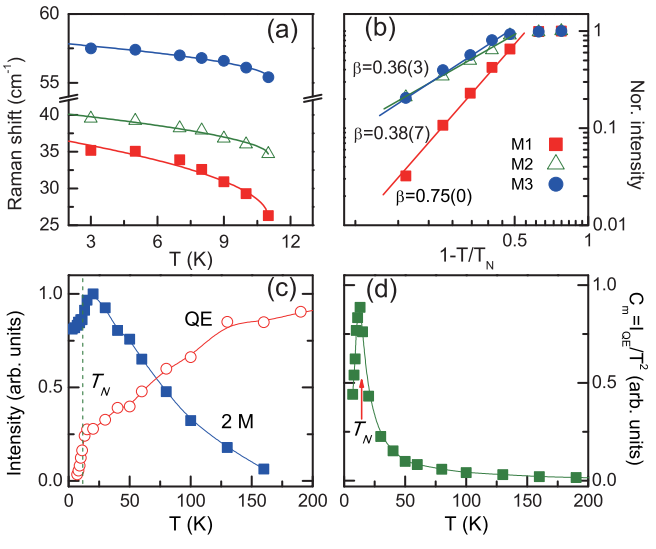

FIG. 10. (Color online) (a) Peak frequency of the magnetic signals, $M_i (i = 1–3)$. See the text for the solid lines. (b) Scattering intensity of M_i on a log-log plot as a function of the reduced temperature, $1 - T/T_N$. (c) Temperature dependence of the scattering intensity of two magnon continuum, $2M$ and quasielastic scattering, QE. (d) Temperature dependence of the magnetic specific heat derived from the intensity of QE normalized by T^2.

Raman scattering yields the temperature dependence of the order parameter M, $I_R \propto M^4 \propto (1 - T/T_N)^{4\beta}$. The critical exponent is evaluated to be $\beta = 0.750 \pm 0.07$, 0.387 ± 0.04, and 0.363 ± 0.09 for the respective M_i ($i = 1$–3). This is evident from a log-log plot of I_R in the reduced temperature, $1 - T/T_N$. β of the M_2 and M_3 mode is very close to $\beta = 0.367$ known for a 3D Heisenberg antiferromagnet. In contrast, the large value $\beta = 0.750 \pm 0.07$ of the M_1 mode, even bigger than a mean-field value $\beta = 0.5$, suggests that the M_1 mode is of different origin from the transverse magnons, M_2 and M_3. A candidate is the excited singlet pertaining to an isolated tetrahedron [20]. The other possibility is the longitudinal magnon whose energy should vanish as the temperature approaches T_N [10]. The M_1 mode undergoes a softening by 10 cm^{-1} but it has a finite energy at T_N. This behavior indicates a weakly first-order transition. It is interesting to note that in Cu2252-Br, hydrostatic pressure can be used to induce a similar softening with aspects of weak first-order behavior [21].

In addition to the sharp excitations discussed above, we have also observed broader signals of magnetic origin, a $2M$ continuum and quasielastic scattering. With increasing temperature the $2M$ scattering intensity increases and even forms a maximum at 20 K, i.e., very close to the maximum in the magnetic susceptibility. The same behavior is observed in the related compound Cu2252. The $2M$ scattering persists to 160 K, implying the persistence of finite-energy short-range spin correlations up to $\approx 12 T_N$. This is consistent with the critical-like broadening of the ESR linewidth in the same temperature range.

The quasielastic Raman scattering originates from either diffusive fluctuations of a four-spin time correlation function or fluctuations of the magnetic energy density [31,32]. Using a hydrodynamic description of the correlation function [33,34], the quasielastic Raman response is approximated by a Lorentzian profile $I_{QE}(\omega) \propto C_m T^2 D_T k^2/[\omega^2 + (D_T k^2)^2]$, where k is the scattering wave vector, D_T is the thermal diffusion constant, and C_m is the magnetic specific heat. Since the scattering intensity of $I_{QE}(T)$ is proportional to $C_m T^2$, the magnetic specific heat is derived from the relation $C_m \propto I_{QE}(T)/T^2$. In Fig. 10(d) the derived C_m is plotted as a function of temperature. We are able to identify a sharp peak at T_N, which is similar to the thermodynamic specific-heat data [6].

IV. DISCUSSION

A direct comparison between Cu45124 and Cu2252 allows examining the influence of dimensionality and crystal symmetry on magnetism in coupled spin tetrahedra systems. The two compounds have similar magnetic parameters. This is nicely demonstrated by the ratio of T_N versus the temperature of susceptibility maximum: $T_N/T_{\chi\,\mathrm{max}} = 0.79$ and 0.72 for Cu2252 and Cu45124, respectively. Here we summarize the key results of the magnetization, ESR, and magnetic Raman-scattering measurements.

Magnetization. In Fig. 11 we compare the $M(H)$ between Cu45124 and Cu2252-Cl measured at the same temperature and orientation. For $H \| c$ and $H \| a$, $M(H)$ of Cu45124 resembles each other except for the low-field spin-flop transition at $\mu_0 H_{\mathrm{SF}} = 16$ T. The rather isotropic magnetization is

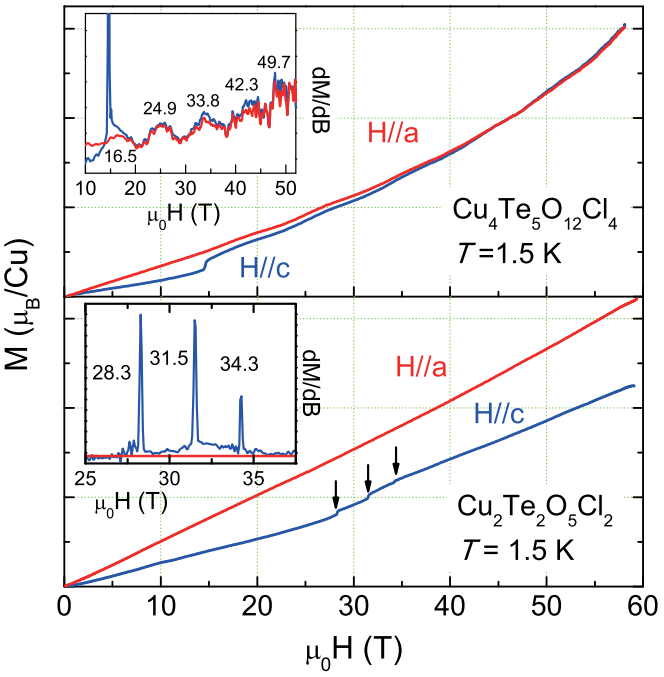

FIG. 11. (Color online) Comparison of the high-field magnetization between Cu45124 (upper panel) and Cu2252-Cl (lower panel) measured at $T = 1.5$ K for $H \| c$ and $H \| a$.

consistent with the more 3D network of the spin tetrahedra in Cu45124. In contrast, Cu2252-Cl shows a very anisotropic magnetization curve between the two orientations: for $H \| a$, $M(B)$ increases almost linearly with H while for $H \| c$, $M(B)$ displays successive, sharp magnetization steps at $\mu_0 H =$ 28.3, 31.5, and 34.3 T. If these are interpreted as successive spin-flop transitions, their energies are almost twice $\mu_0 H_{\mathrm{SF}} =$ 16 T of Cu45124. This ascertains that Cu2252 has strong anisotropic intertetrahedral interactions.

ESR. As compared in Fig. 12(a), in the paramagnetic phase the ESR linewidth is $\Delta B_{pp}(300\ \mathrm{K}) = 1.635 \pm 0.004$ T for Cu45124 and 1.823 ± 0.009 T for Cu2252. The ESR spectrum becomes broader by 10% for Cu2252 than for Cu45124. This is related to the increase of the intratetrahedral interactions [23]. In the AFM phase the sharp AFMR mode is observed for Cu45124, which follows a classical behavior. In contrast, a well-defined AFMR mode cannot be probed for Cu2252 in the used frequency and field range [see the red line in Fig. 12(a)]. This might be due to a huge magnon gap as indicated by the large spin-flop field amounting to about 31 T.

Magnetic Raman excitations. As summarized in Fig. 12(b), Cu45124 has three sharp magnetic modes at 35 (M_1), 40 (M_2), and 57 cm^{-1} (M_3), while Cu2252 has four magnetic modes at 23 (M_1), 39 (M_2), 49 (M_3), and 67 cm^{-1} (M_4) [20]. In addition, there appears a broad two-magnon continuum extending from 20 to 130 cm^{-1}. The center position of the continuum is $E_m = 72$ cm^{-1} for Cu45124 and $E_m = 81$ cm^{-1} for Cu2252. The magnetic energy and spectral weight shifts by 10% to higher energy for Cu2252. This scales with the strength of the intratetrahedra interactions and is consistent with the increase of the ESR linewidth by the same amount.

Taking the above results together, our thermodynamic and spectroscopic data demonstrate that Cu45124 behaves like a

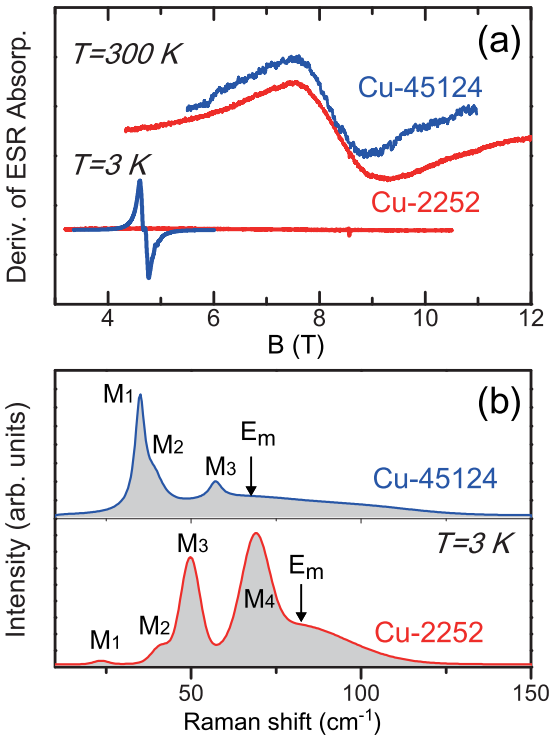

FIG. 12. (Color online) Comparison of ESR between Cu45124 (blue line) and Cu2252 (red line) in a paramagnetic phase at $T = 300$ K and in an antiferromagnetic phase at $T = 3$ K. (b) Comparison of magnetic Raman spectra between Cu45124 (upper panel) and Cu2252 (lower panel) at $T = 3$ K.

three-dimensional antiferromagnet: (i) the spin-flop transition at $\mu_0 H_{SF} = 16$ T in the magnetization curve, (ii) the AFMR mode following the T dependence $\Delta B_{pp}(T) \propto T^{3.13\pm0.04}$ expected for a classical magnet, and (iii) the transverse magnon M_2 and M_3 modes whose intensities display an order parameter of a 3D Heisenberg antiferromagnet. This is further supported by the first-principle calculations [23], which disclosed a three-dimensional arrangement of spin tetrahedra. However, detailed features cannot be captured within a conventional 3D antiferromagnet.

Significantly, there are experimental indications that an isolated tetrahedron related physics is not totally exhausted in spite of 3D interactions. The periodic magnetization jumps and the T dependence of the M_1 mode are taken as a signature from the quantized energy bands and singlet fluctuations. Although the 3D interactions broaden the energy levels of the spin tetrahedra, each band does not fully overlap at least in the low-energy regime. The crossover to a 3D classical magnet is not yet completed and thus the remnant of 0D feature is still visible. Cu45124 exhibits both localized and collective magnetism in thermodynamic and spectroscopic measurements.

These observations are in stark contrast to Cu2252. Neither the periodic magnetization jumps nor the conventional AFMR mode are observed. Rather, the anisotropic magnetization curves and the large spin-flop field advocate a more anisotropic magnetic structure with the increased quasi-one dimensionality. This is supported by the first-principle calculations [23], which showed pronounced in-plane diagonal intertetrahedral interactions relative to out-of-plane ones. Thus, we conclude that the difference of magnetism between Cu45124 and Cu2252 is mainly dictated by the nature of intertetrahedral exchange interactions: more 3D intertetrahedral interactions for Cu4512 vs more 1D (or 2D) intertetrahedral interactions for Cu2252. The lower connection of the spin tetrahedra in Cu2252 partly explains why a mean-field or random-phase approximation failed to reproduce the size and intensity of the gapped excitations probed by inelastic neutron scattering [4,18]. Given that Cu4512 lies proximate to a mean-field limit, we propose to test the validity of a mean-field theory to account for low-lying excitations using inelastic neutron-scattering experiments.

V. CONCLUSION

We have presented a combined high-field magnetization, high-frequency ESR, and Raman-scattering study of the coupled spin-tetrahedra system $Cu_4Te_5O_{12}Cl_4$. Our thermodynamic and spectroscopic data reveal the many-sided aspects of coupled spin-tetrahedra magnetism that cannot be fully disclosed in the related compound $Cu_2Te_2O_5Cl_2$ due to anisotropic spin-tetrahedra connections. In the case of $Cu_4Te_5O_{12}Cl_4$, the three-dimensionally isotropic network of spin tetrahedra with reduced in-plane intertetrahedral couplings places the studied system closer to a 3D coupled spin tetrahedra system, rendering the observation of both zero-dimensional quantized and three-dimensional collective magnetic behaviors. The observed coexistence is not well understood by current existing theories. While further studies are needed to obtain a unified picture of a crossover from zero- and three-dimensional physics, $Cu_4Te_5O_{12}Cl_4$ is an interesting class of 3D coupled zero-dimensional materials.

ACKNOWLEDGMENTS

This work was supported by Basic Science Research Program through the National Research Foundation of Korea (NRF) funded by the Ministry of Education, Science and Technology (Grants No. 2012-046138, No. 2012R1A2A1A03005174, and No. 2013R1A1A2007959) as well as by German-Israeli Foundation (GIF, 1171-486 189.14/2011), the NTH-School "Contacts in Nanosystems: Interactions, Control and Quantum Dynamics," the Braunschweig International Graduate School of Metrology, and DFG-RTG 1953/1, Metrology for Complex Nanosystems. A portion of this work was performed at the National High Magnetic Field Laboratory, which is supported by the NSF Cooperative Agreement No. DMR-0654118, and by the State of Florida. Pulsed field experiments are supported by EuroMagNET II under EC Contract No. 228043.

[1] P. Lemmens, K.-Y. Choi, E. E. Kaul, C. Geibel, K. Becker, W. Brenig, R. Valenti, C. Gros, M. Johnsson, P. Millet, and F. Mila, Phys. Rev. Lett. **87**, 227201 (2001).

[2] K. Totsuka and H.-J. Mikeska, Phys. Rev. B **66**, 054435 (2002).

[3] W. Brenig, Phys. Rev. B **67**, 064402 (2003).

[4] K. Prsa, H. M. Rønnow, O. Zaharko, N. B. Christensen, J. Jensen, J. Chang, S. Streule, M. Jiménez-Ruiz, H. Berger, M. Prester, and J. Mesot, Phys. Rev. Lett. **102**, 177202 (2009).

[5] M. Johnsson, K. W. Tornroos, F. Mila, and P. Millet, Chem. Mater. **12**, 2853 (2000).
[6] R. Takagi, M. Johnsson, V. Gnezdilov, R. K. Kremer, W. Brenig, and P. Lemmens, Phys. Rev. B **74**, 014413 (2006).
[7] I. Zivković, D. M. Djokić, M. Herak, D. Pajić, K. Prsa, P. Pattison, D. Dominko, Z. Micković, D. Cincić, L. Forró, H. Berger, and H. M. Rønnow, Phys. Rev. B **86**, 054405 (2012).
[8] M. Fujihala, X.-G. Zheng, H. Morodomi, T. Kawae, and I. Watanabe, Phys. Rev. B **87**, 144425 (2013).
[9] P. Lemmens, K.-Y. Choi, A. Ionescu, J. Pommer, G. Guntherodt, R. Valenti, C. Gros, W. Brenig, M. Johnsson, P. Millet, and F. Mila, J. Phys. Chem. Solids **63**, 1115 (2002).
[10] C. Gros, P. Lemmens, M. Vojta, R. Valenti, K.-Y. Choi, H. Kageyama, Z. Hiroi, N. V. Mushnikov, T. Goto, M. Johnsson, and P. Millet, Phys. Rev. B **67**, 174405 (2003).
[11] R. Valenti, T. Saha-Dasgupta, C. Gros, and H. Rosner, Phys. Rev. B **67**, 245110 (2003).
[12] J. Jensen, P. Lemmens, and C. Gros, Europhys. Lett. **64**, 689 (2003).
[13] O. Zaharko, A. Daoud-Aladine, S. Streule, J. Mesot, P.-J. Brown, and H. Berger, Phys. Rev. Lett. **93**, 217206 (2004).
[14] M. Prester, A. Smontara, I. Zivkovic, A. Bilusic, D. Drobac, H. Berger, and F. Bussy, Phys. Rev. B **69**, 180401(R) (2004).
[15] J. Kreitlow, S. Sullow, D. Menzel, J. Schoenes, P. Lemmens, and M. Johnsson, J. Magn. Magn. Mater. **290-291**, 959 (2005).
[16] X. Wang, I. Loa, K. Syassen, P. Lemmens, M. Hanfland, and M. Johnsson, J. Phys.: Condens. Matter **17**, 807 (2005).
[17] O. Zaharko, H. Rønnow, J. Mesot, S. J. Crowe, P. J. Brown, A. Daoud-Aladine, A. Meents, A. Wagner, M. Prester, H. Berger, and D. M. Paul, Phys. Rev. B **73**, 064422 (2006).
[18] S. J. Crowe, S. Majumdar, M. R. Lees, D. McK. Paul, R. I. Bewley, S. J. Levett, and C. Ritter, Phys. Rev. B **71**, 224430 (2005).
[19] S. J. Crowe, M. R. Lees, D. M. Paul, R. I. Bewley, J. Taylor, G. McIntyre, O. Zaharko, and H. Berger, Phys. Rev. B **73**, 144410 (2006).
[20] K.-Y. Choi, H. Nojiri, N. S. Dalal, H. Berger, W. Brenig, and P. Lemmens, Phys. Rev. B **79**, 024416 (2009).
[21] X. Wang, K. Syassen, M. Johnsson, R. Moessner, K.-Y. Choi, and P. Lemmens, Phys. Rev. B **83**, 134403 (2011).
[22] S.-H. Baek, K.-Y. Choi, H. Berger, B. Büchner, and H.-J. Grafe, Phys. Rev. B **86**, 180405 (2012).
[23] B. Rahaman, H. O. Jeschke, R. Valenti, and T. Saha-Dasgupta, Phys. Rev. B **75**, 024404 (2007).
[24] K.-Y. Choi, Z. Wang, A. Ozarowski, J. van Tol, H. D. Zhou, C. R. Wiebe, Y. Skourski, and N. S. Dalal, J. Phys.: Condens. Matter **24**, 246001 (2012).
[25] D. Wulferding, K.-Y. Choi, P. Lemmens, A. N. Ponomaryov, J. van Tol, A. T. M. Nazmul Islam, S. Toth, and B. Lake, J. Phys.: Condens. Matter **24**, 435604 (2012).
[26] K.-Y. Choi, I. H. Choi, P. Lemmens, J. van Tol, and H. Berger, J. Phys.: Condens. Matter **26**, 086001 (2014).
[27] S. M. Rezende and R. M. White, Phys. Rev. B **14**, 2939 (1976).
[28] M. Balkanski, R. F. Wallis, and E. Haro, Phys. Rev. B **28**, 1928 (1983).
[29] W. Hayes and R. Loudon, *Scattering of Light by Crystals* (Dover, New York, 2012).
[30] P. Lemmens, G. Guntherodt, and C. Gros, Phys. Rep. **375**, 1 (2003), and references therein.
[31] G. F. Reiter, Phys. Rev. B **13**, 169 (1976).
[32] J. W. Halley, Phys. Rev. Lett. **41**, 1605 (1978).
[33] B. I. Halperin and P. C. Hohenberg, Phys. Rev. **188**, 898 (1969).
[34] K.-Y. Choi, P. Lemmens, and H. Berger, Phys. Rev. B **83**, 174413 (2011).